Original Article

Computational analysis of drug free silver triangular nanoprism theranostic probe plasmonic behavior for in-situ tumor imaging and photothermal therapy

Sudip Mondal [a], José Luis Montaño-Priede [b,1], Van Tu Nguyen [c], Sumin Park [c], Jaeyeop Choi [c], Vu Hoang Minh Doan [c], Thi Mai Thien Vo [c], Tan Hung Vo [c], Nicolas Large [b], Chang-Seok Kim [d], Junghwan Oh [a,b,e,*]

[a] New-senior Healthcare Innovation Center (BK21 Plus), Pukyong National University, Busan 48513, Republic of Korea
[b] Department of Physics and Astronomy, The University of Texas at San Antonio, One UTSA Circle, San Antonio, Texas 78249, United States
[c] Industry 4.0 Convergence Bionics Engineering, Department of Biomedical Engineering, Pukyong National University, Busan 48513, Republic of Korea
[d] Department of Cogno-Mechatronics Engineering, Pusan National University, Busan 46241, Republic of Korea
[e] Ohlabs Corp., Busan 48513, Republic of Korea

HIGHLIGHTS

- Designing drug-free polyvinyl alcohol coated stable silver triangular nano-prisms (PVA-SNT).
- Computational simulation of optical and photothermal properties with high in vivo experimental similarity.
- Stable PVA-SNT enables photoacoustic imaging-guided photothermal therapy of breast cancer.
- PVA-SNT exhibits enhanced photostability and high photothermal conversion efficiency.

GRAPHICAL ABSTRACT
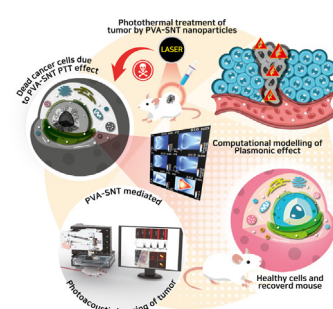
ARTICLE INFO

ABSTRACT

Introduction: The advanced features of plasmonic nanomaterials enable initial high accuracy detection with different therapeutic intervention. Computational simulations could estimate the plasmonic heat generation with a high accuracy and could be reliably compared to experimental results. This proposed combined theoretical-experimental strategy may help researchers to better understand other nanoparticles in terms of plasmonic efficiency and usability for future nano-theranostic research.

Objectives: To develop innovative computationally-driven approach to quantify any plasmonic nanoparticles photothermal efficiency and effects before their use as therapeutic agents.

Methods: This report introduces drug free plasmonic silver triangular nanoprisms coated with polyvinyl alcohol biopolymer (PVA-SNT), for in vivo photoacoustic imaging (PAI) guided photothermal treatment (PTT) of triple-negative breast cancer mouse models. The synthesized PVA-SNT nanoparticles were characterized and a computational electrodynamic analysis was performed to evaluate and predict the optical and plasmonic photothermal properties. The in vitro biocompatibility and in vivo tumor abalation study was performed with MDA-MB-231 human breast cancer cell line and in nude mice model.

Results: The drug free 140 μg·mL^{-1} PVA-SNT nanoparticles with 1.0 W·cm^{-2} laser irradiation for 7 min proved to be an effective and optimized theranostic approach in terms of PAI guided triple negative breast cancer treatment. The PVA-SNT nanoparticles exhibits excellent biosafety, photostability, and strong efficiency as PAI contrast agent to visualize tumors. Histological analysis and fluorescence-assisted cell shorter assay results post-treatment apoptotic cells, more importantly, it shows substantial damage to in vivo tumor tissues, killing almost all affected cells, with no recurrence.

Conclusion: This is a first complete study on computational simulations to estimate the plasmonic heat generation followed by drug free plasmonic PAI guided PTT for cancer treatment. This computationally-driven theranostic approach demonstrates an innovative thought regarding the nanoparticles shape, size, concentration, and composition which could be useful for the prediction of photothermal heat generation in precise nanomedicine applications.

Introduction

Individuals born with intensely personal genomic structure may be at increased risk of cancer during their life due to multiple triggering factors. The future of disease management, including cancer, is largely dependent on advanced personalized nanomedicine [1]. The advanced features of nanomaterials facilitate early detection with high precision and minimal invasion [2]. The recent approach of theranostic allows nanomedicine to co-load with drugs and contrast agents for concurrent imaging and therapy [3–5]. This strategy helps guiding the visualization of target site, quantification of drug accumulation, and treatment progress. However, associated drugs may often cause collateral damages to non-cancerous cells [6]. During clinical applications in patients, these formulations are more difficult to translate and their performance does not meet the expected medical standards. Presently, radiotherapy and chemotherapy are the two commonly used therapeutic approaches for cancer treatment. Radiotherapy not only kills or slows the growth of cancer cells, it can also affect surrounding healthy cells which results several side effects. On the contrary chemotherapeutic agents result in collateral damage to non-cancerous cells *via* oxidative stress or fatal side effects [7]. An alternative to these treatments is plasmonic photothermal therapy [8]. This effective cancer therapeutics is based on the irradiation of metallic nanoparticles (NPs) with a near-infrared (NIR) laser for the excitation of a collective and coherent oscillation of their conduction electrons, known as localized surface plasmon resonance (LSPR) [7]. Noble metals, such as gold and silver, show very strong optical absorption and scattering in the visible and NIR regions [9,10]. Techniques such as surface-enhanced Raman scattering (SERS), dark-field microscopy, and photoacoustic microscopy are used for such non-invasive nanoparticle detection purpose [11,12]. Theranostic probe could represent a personalized medicine by integrating tailored optical properties in nanomaterials with photothermal (*i.e.*, hyperthermia) efficiency [13,14]. The efficient photothermal effect which allows for light-to-heat conversion by noble metal nanoparticles is a promising technique for hyperthermia-mediated tumor management [15,16]. These versatile optical properties, allow these nanoparticles to be used in different biomedical applications such as photothermal treatment [8,17], surface-enhanced Raman spectroscopy [18,19], sensing [20,21], and photocatalysis [22,23]. Upon optical excitation close to their LSPR, metallic nanoparticles induce intense and strongly localized electric fields at their surface. The strong concentration of electromagnetic energy in the nanoparticle and its vicinity results in a significant temperature increase inside the nanoparticle as well as in its surrounding environment [23–27]. Fig. 1a, which reports a direct comparison of the quality factors of various plasmonic metals in the wavelength range 200–1200 nm, clearly shows in entire spectrum (300–1200 nm) Ag shows the highest quality factor [28]. "Al" is only suitable for applications in the visible and ultraviolet (UV) ranges. Interband transitions also play an

important role in dampening the surface plasmon modes [29]. In the case of Ag, interband transitions take place at much higher frequencies compared to Au and Cu, for which their LSPR to wavelength transitions were limited by longer than 500 and 600 nm respectively [30].

Along with fabrication limitations, the materials cost is another burden for plasmonic research. As of today, there is a significant cost variance among the metals which can sustain plasmonic effects [25,31]. Au and Ag are the most widely used plasmonic materials as they offer unequaled optical properties. The use of Ag over the other metals appears to be the best option as it combines good qualities in terms of plasmonic ability (high spectral tunability and quality factor), well-known synthesis with high control over size and morphology, and cost-effectiveness [31–35] (see Supporting Information Table S1). Contrary to gold, the prime concern with Ag NPs, which limits their application in biomedicine, is associated with their stability [36]. The stability of Ag NPs could be improved by chemically passivating the nanoparticle surface with a polymer, ceramics, or biomolecular coating [37,38]. Till date different biopolymers such as polyethylene glycol (PEG), polyvinylpyrrolidone (PVP), polylactic acid (PLA), polycaprolactone (PCL), collagen, chitosan, gelatin, glycogen etc. are used for nanoparticles coating purposes [39]. Among widely used biopolymers, polyvinyl alcohol (PVA) is the most popular synthetic polymer due to its water solubility, non-toxicity, and high stability. PVA is more environmental friendly polymer, containing pendant hydroxyl groups in its simple structure which makes it most bioabsorbable material [40]. PVA is often used in skin tissue engineering, drug delivery, wound and burn healing, artificial cornea, and contact lens fabrication [41]. Ag NPs surface could adsorb the PVA through multiple chemical activities, among which noncovalent bonding of the hydroxyl group is the most important interaction [42]. To date very few reports are available with silver triangular nanoprisms (SNT)-mediated photothermal therapy for cancer treatment. Boca-Farcau *et al.* reported SERS-labeled silver nanotriangles conjugated with folic acid for the multimodal detection and targeted photothermal treatment on human ovarian cancer cells [13]. However, this study lacks of in vivo application as they present an in vitro study only. Homan et al. PEGylated Ag nanoplates only for in vivo molecular photoacoustic imaging. No tumor treatment study was performed [43]. Whereas, Liu et al. reported surface plasmon properties of hollow AuAg alloyed triangular nano-boxes and their applications in SERS imaging and drug delivery. This study lack of tumor inducing and their treatment [44]. Our study reports Photoacoustic imaging guided photothermal therapy for cancer treatment. In a recent study by Zeng et al. reported a stable biocompatible silver nanoprism–polydopamine (PDA) core–shell nanoplatform loaded with doxorubicin drug for targeted drug delivery and tumor imaging through PA/IRT/CT. The nanoplatform further used for PTT mediated tumor treatment. Compared to our present study this reported study devoid of com-
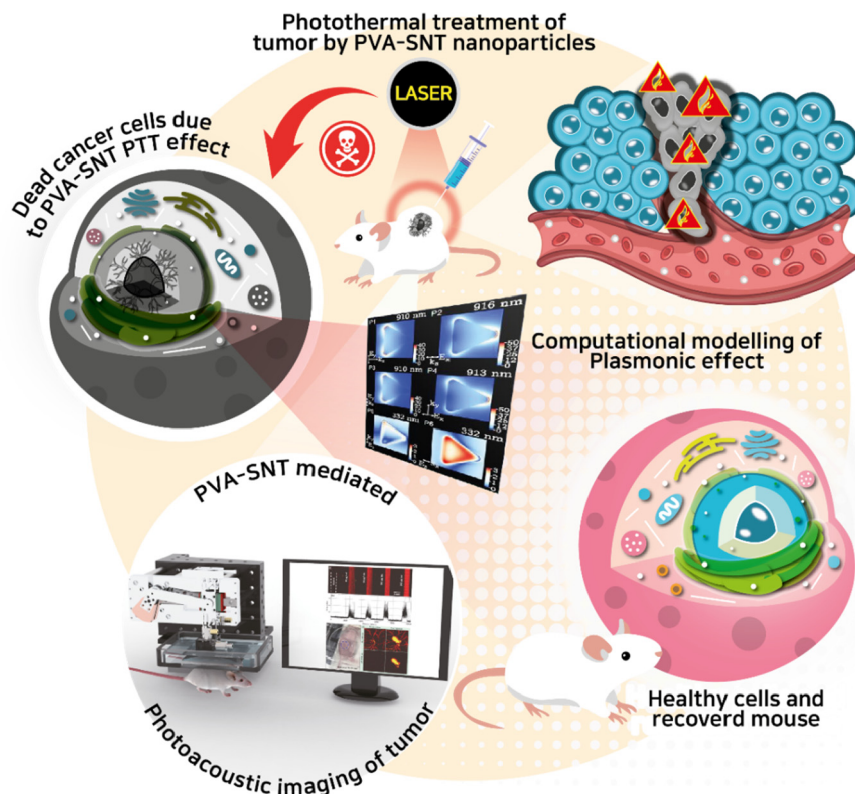
Scheme 1. Schematic representation of plasmonic silver triangular nanoprism (PVA-SNT) theranostic probe for tumor imaging and photothermal therapy.

putational electrodynamic analysis to evaluate plasmonic photothermal properties [45].

In general, the laser penetration efficiency of PTT is limited to few millimeters under the skin level, which is better accessible by subcutaneous injection. Intravenous (IV) injection administration is the advanced clinical option to deliver drug or therapeutic agents specifically targeted to the affected tissues. To achieve this property nanoparticles are conjugated or modified with specific targeted agents/ molecules. Unfortunately, most of the nanoparticles bind to nonspecific sites or tissues, which often results in collateral damages to non-cancerous cells. In real-time clinical applications, these formulations are more difficult to translate and their performance does not meet the expected medical standards.

Here, we focused on NIR I level laser source to counter the subcutaneous tumor by local intra-tumoral intervention. This process is a far safer method for subcutaneous level anomalies such as basal cell carcinoma, squamous cell carcinoma, follicular lymphoma, Merkle cell cancer, and melanoma. The study aims to synthesize stable PVA-coated silver triangular nanoprisms (PVA-SNT) as a theranostic agent for biomedical imaging guided cancer therapy. The approach of our study relies on the use of theoretical and computational electrodynamics and heat transfer simulations to calculate the nanoparticles optical properties and estimate the plasmonic heat generation, and guide our wet chemical experimental study with in vitro and in vivo applications for the treatment of triple negative breast cancer mouse model (Scheme 1).

Experimental

Materials and methods

All the chemicals were purchased from Sigma Aldrich (St. Louis, MO, USA). Dulbecco's modified Eagle's medium (DMEM), fetal

bovine serum (FBS), antibiotic, trypsin, and phosphate-buffered saline (PBS) were purchased from HyClone (South Logan, UT, USA). Annexin V-FITC apoptosis detection kit (BD Pharmingen, San Jose, CA, USA). Deionized water (DI) of $\rho > 18.2$ $\Omega\cdot$cm (at 25 °C) from a Millipore deionizer was used during the entire experimental study.

Synthesis of PVA-SNT

The silver triangular nanoprisms coated with polyvinyl alcohol were synthesized by a dynamic chemical method with a modification of a previous protocol [46]. Briefly, 30 mL of 0.2 M polyvinyl alcohol aqueous solution was prepared and subsequently AgNO$_3$ (450 μL, 0.01 M) solution added. Stirring for 5 min at room temperature (25 ± 2 °C), then 600 μL of 0.1 M sodium citrate was added. Next, 300 μL of 30 wt% H$_2$O$_2$ was added to the solution stirred in a magnetic stirrer (400 rpm for 8 min). A freshly prepared 400 μL NaBH$_4$ (100 mM) solution was added into the existing solution, resulting in a color change of the solution from transparent to yellow. Finally, an additional 180 μL of H$_2$O$_2$ was added, which gradually changes the reaction color from yellow to red, and finally to dark blue, indicating the formation of PVA-coated silver triangular nanoprisms. The same synthesis procedure was followed to synthesize SNT nanoparticles, where, deionized (DI) water was used in place of the PVA solution. The resulting PVA-SNT and SNT nanoparticles were centrifuged at 14,000 rpm for 6 min at 4 °C. After discarding the liquid phase, a 0.2 M PVA solution was again added to re-suspend the PVA-SNT nanoparticles, whereas, only DI water was used to re-suspend the SNT nanoparticles. Finally, the synthesized PVA-SNT and SNT nanostructures were kept at 4 °C for future use.

Characterization

The physico-chemical properties of the nanomaterials were characterized using field emission transmission electron

microscopy (FETEM, JEM-2100F; JEOL, Tokyo, Japan) and energy-dispersive X-ray spectroscopy (EDS). The absorbance spectra of the synthesized SNT and PVA-SNT were acquired using an ultraviolet–visible (UV–vis) spectrophotometer (Genesys 30S; Thermo Fisher Scientific, Waltham, MA, USA). X-ray photoelectron spectroscopy (XPS) was carried out using an AXIS Supra electron spectrometer (Kratos Analytical Ltd., Manchester, UK). The binding energies (BE) were determined with an accuracy of ± 0.1 eV. The deconvolution of the peaks was performed using ESCApe™ from Kratos Analytical Ltd., Manchester, UK. The functional groups for PVA, SNT, and PVA-SNT were determined by using Fourier-transform infrared spectroscopy (FTIR, JASCO FRIT 4100). Dynamic light scattering (DLS) and surface zeta potential (ZP) measurements of the nanomaterials were performed using an electrophoretic light scattering spectrophotometer (ELS-8000; Otsuka Electronics Co. Ltd., Osaka, Japan). The silver ion concentration of the nanostructures was quantified by an inductively coupled plasma mass spectrometer (ICP-MS; PerkinElmer-NexION 300D, PerkinElmer, Inc., USA). A NIR laser at 808 nm (Changchun New Industries Optoelectronics Technology, Changchun, China) was used to conduct the photothermal experiments, and the thermographs were recorded using a digital IR thermal imaging camera (FLIR Systems Inc., Portland, OR, USA). A photoacoustic microscopy (PAM) system (FPAM-v1, Ohlabs Inc., Busan, South Korea) was used to perform in vitro and in vivo photoacoustic imaging. All the raw data were processed in MATLAB to generate PA images.

Flow cytometry analysis of cell death

The seeded cells were incubated with PVA-SNT for 6 h and treated with an 808-nm laser at 1.0 W·cm^{-2} for 5 min. Photothermally treated cells (except control) were incubated for 6 h at 37 °C in a CO$_2$ incubator. Post PTT live and dead cells were harvested and washed with cold PBS, followed by staining with Annexin V-FITC apoptosis detection kit. The flow cytometry experimental study was performed with a BD FACSVerse flow cytometer (BD Biosciences, CA, USA). The final results were acquired and analyzed using FlowJo (Ashland, OR, USA).

Animal model

A group of female BALB/c nude mice (18.9 ± 0.8 g), with six to seven weeks age were procured from Orient Bio Inc. (Seongnam, Republic of Korea). After one day interval the treatment group mice were injected (subcutaneously into the flanks region) with MDA-MB-231 cells (10^6 cells) suspended in 100 μL of PBS. The animals were kept under normal room temperature condition with regular care until the tumors reached a volume of ~100 mm^3. The animals were then divided into four groups. A total of 12 animals were studied for this experiment, as detailed in Supporting Information Table S2.

The tumor-bearing mice were intratumorally injected with 100 μL of a 140 μg·mL^{-1} PVA-SNT nanoparticle solution. Next the mice were kept in proper environment with regular monitoring until the operative tumor volume reached approximately 1 cm^3. The tumor of each mouse was irradiated by an optical fiber coupled to a 808 nm laser diode at 1.0 W·cm^{-2} for 7 min. All four groups, which include (I) untreated mice without any tumor (control group), (II) tumor induced mice exposed to the laser (only laser exposure, no nanoparticles injected), (III) the mice intratumor injected with PVA-SNT nanoparticles (without laser exposure), and (IV) PVA-SNT intra-tumor injected mice with laser irradiation. A probe thermocouple was placed on the tumor central region to estimate the temperature during the experimental irradiation with 1 s interval.

Ethics statement

All experiments involving animals were conducted according to the ethical policies and procedures approved by the Ethical Committee of Pukyong National University, Busan, (Approval no. PKNUIACUC-2019-05), and also followed the Animal Ethical Policies of the Republic of Korea.

Histological analysis

At the end of the 3-week treatment (treatment started after day 28, when the tumor grew to the appropriate size) and observation, the mice from each group were sacrificed and we collected five major organs (liver, spleen, kidney, lungs, and heart) and the tumor. The collected organs were rinsed with saline water and kept in 10% formalin for fixation and staining. After a 24 h immersion, the tissues were fixed with paraffin and 4 μm thick sections were collected for hematoxylin and eosin (H&E) staining. Finally, the slices were visualized in an optical microscope.

Photoacoustic imaging (PAI) & in vivo photothermal therapy

Noninvasive biomedical imaging techniques have recently emerged as a promising diagnosis technique. Among the different imaging techniques, PAI has the potential ability to detect and quantify nanoparticle contrast agents inside the body systems. An in vitro and in vivo photoacoustic microscopy system (FPAM-v1, Ohlabs, Busan, South Korea) was used as detailed in an earlier report [47]. For in vitro PAI, MDA-MB-231 cells were incubated with different concentrations of PVA-SNT (20, 60, 100, and 140 μg·mL^{-1} of PVA-SNT) at 37 °C for 6 h. After trypsin digestion, the cells were collected by centrifugation at 1200 rpm for 4 min. Finally, the cell pellets were collected into a polytetrafluoroethylene (PTFE) tube (Zeus) for photoacoustic imaging. MDA-MB-231 tumor-bearing nude mice were intratumorally injected with PVA-SNT (140 μg·mL^{-1}) for PAI. Post-injection scanning of the entire tumor region was performed using a FPAM-v1 system [48]. Also, a control group only with DI water (without nanoparticles) was used for a comparative study.

Statistical analysis

All the data were expressed as the mean ± standard deviation. Statistical analyses were carried out using one-way analysis of variance. OriginPro 8.0 from OriginLab corp. (Northampton, MA, USA) was used to analyze the data.

Results and discussion

UV–visible spectroscopy analysis

The color change of the transparent silver ion precursors to AgNPs can be visually observed. The UV–vis absorbance peaks help to identify the possible morphology and size distribution of the synthesized nanoparticles. A characteristic band appears below 320 nm due to the $4d \rightarrow 5sp$ interbrand transitions in silver [49]. The plasmonic response of AgNPs is then visible at wavelengths beyond 350 nm; the exact position of the LSPRs depends on the nanoparticle size, shape, dielectric environment, and interparticle interactions [49]. For SNT, the formation of a very broad absorption peak was observed (400–1200 nm) with a visible blue color emission (Fig. 1b,c), consistent with previous works [50].

Transmission electron microscopy (TEM)

TEM study is important to reveal valuable information about the nanostructure and composition [50]. While the synthesized nanoparticles were initially considered to have a triangular morphology, the in-depth analysis revealed that the edges of the triangular prisms are not sharp (Fig. 1d, e). Additionally, a mixture of

hexagonal and spherical nanoparticles was observed along with the triangular nanoprisms. Post photothermal FE-TEM analysis revealed negligible shape deformation of the PVA-SNT nanoparticles. A detailed morphological study with size distribution is summarized in Table 1. The synthesized SNT revealed an average particle size of 44.5 ± 18 nm. The PVA-SNT nanoparticles exhibit a coating of PVA of ~3 nm over the triangular surface (Fig. 1d). The EDS analysis of SNT confirmed that the synthesized nanoparticles are composed of silver. The peaks at approximately 8 and 9 keV correspond to the Cu K_α and Cu K_β emissions from the TEM copper grid, respectively (see Fig. S1, Supporting Information). The selected area electron diffraction (SAED) pattern reveals the concentric diffraction rings with bright spots corresponding to the (100), (200), (220), and (311) silver lattice planes (Fig. 1f). The HR-TEM analysis revealed an atomic distance of 2.3 Å, which corresponds to the silver (111) plane (Fig. 1g). The functional groups for PVA and PVA-SNT nanoparticles were identified by FTIR analysis (see Fig. S2, Supporting Information).

X-ray photoelectron spectrometry (XPS)

XPS study was performed to detect the surface composition of PVA and PVA-SNT nanoparticles. The XPS survey spectrum of pure PVA (Fig. 1h) revealed two strong binding energies of 294 and 541 eV. For PVA-SNT similar O1s and C1s peaks were identified in the XPS survey spectrum (Fig. 1i) in addition to the Ag 3d peak. Finally, the Ag 3d XPS spectrum revealed two peaks at 374.6 and 368.6 eV, corresponding to the Ag $3d_{3/2}$ and $3d_{5/2}$ of metallic Ag^0 (Fig. 1j).

X-ray diffraction (XRD)

XRD study helps to determine the crystalline structure and nature of the silver material. The X-ray diffraction peaks, which were recorded at 2θ value of 38.46, 45.14, 64.67, and 77.83°, correspond to (111), (200), (220), and (311) lattice planes, respectively, for the face-centered cubic (fcc) structure of silver, (ICDD card No.

Table 1
Average size, standard deviation, number of nanoparticles, and concentrations used for the electrodynamic simulations of NT, NH, and NS.
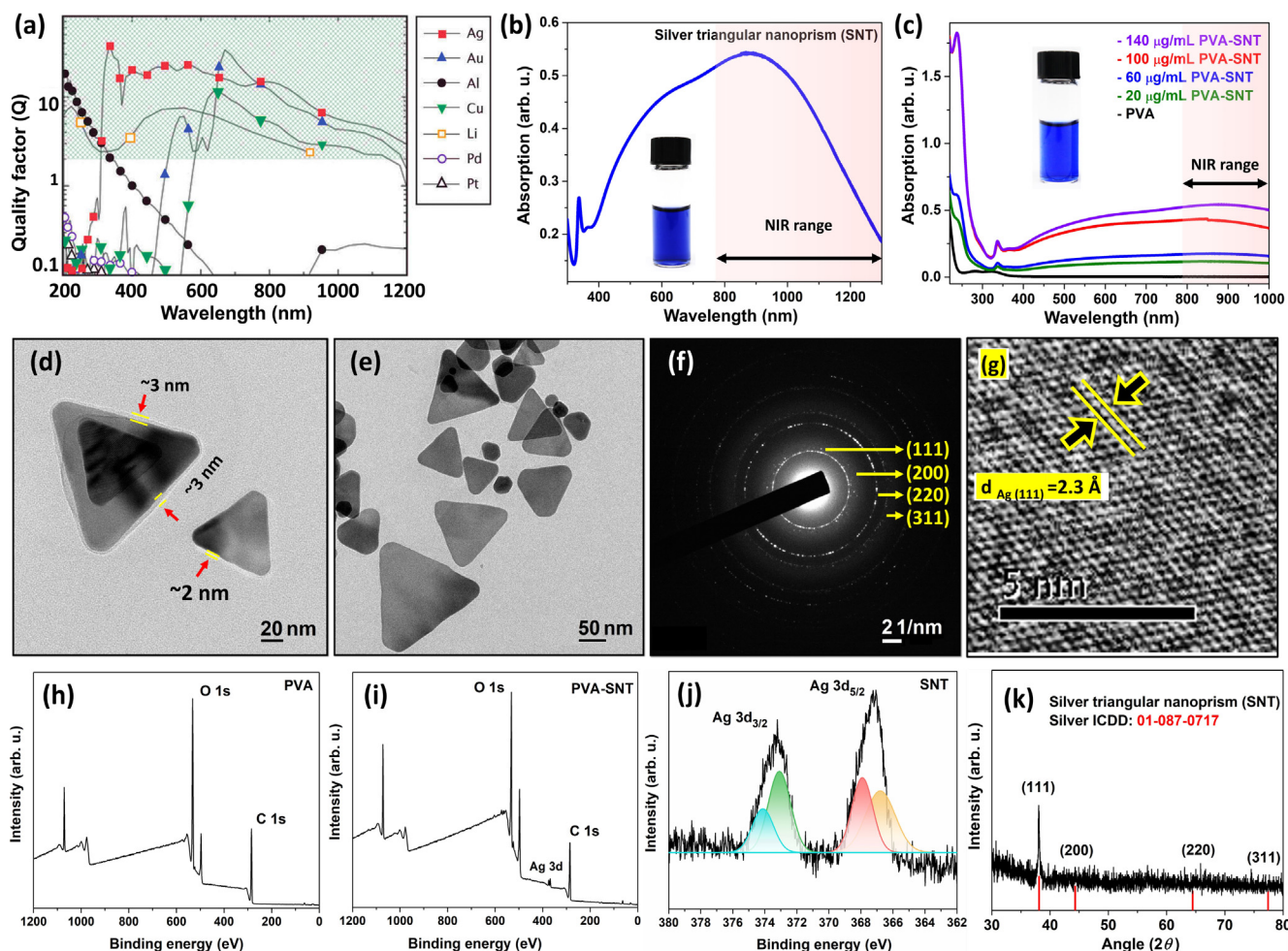
Nanostructure	Average size [nm]	σ [nm]	Number	n_{part}, sim. 1 [NPs μm^{-3}]	n_{part}, sim. 2 [NPs μm^{-3}]
NT	44.5	18	100	30	90
NH	53.5	39	40	12	36
NS	13.1	1.9	70	21	63

Fig. 1. (a) Quality factor (Q) of the LSPR for a metal/air interface. A higher Q denotes less damping and a stronger plasmon resonance. The shaded area represents the region of interest for many plasmonic applications. Reproduced with permission [28] Copyright 2009, Elsevier. (b) UV–vis spectra of synthesized SNT. (c) UV–vis spectra of PVA and different PVA-SNT nanoparticle concentrations. (d) FE-TEM analysis of synthesized SNT. (e) FE-TEM analysis of synthesized PVA-SNT. (f) SAED pattern. (g) HR-TEM analysis of SNT. (h, i) XPS survey spectra of PVA and PVA-SNT material, respectively. (j) High resolution SNT Ag 3d XPS spectrum. (k) XRD analysis of SNT.

01-087-0717) [51]. The calculated interplanar spacing (d_{cal}) values are 2.334, 1.952, 1.429, and 1.221 Å for the (1 1 1), (2 0 0), (2 2 0), and (3 1 1) planes, respectively, and are well correlated with silver (Fig. 1k).

### Nanoparticles stability determination (Zeta potential, zeta size calculation)

The synthesized SNT and PVA-SNT nanoparticles were further studied for zeta potential and hydrodynamic particle size distribution. The synthesized SNT revealed a zeta potential of about −21.37 mV with a hydrodynamic size of about 56.1 ± 2.7 nm. The hydrodynamic size obtained for the PVA-SNT nanoparticles was 63.6 ± 2.9 nm, while the recorded zeta potential was negative (-3.84 mV) due to the PVA coating. The zeta potential study also confirms the coating of PVA polymer over the silver triangular nanoprism. We further extend our research to study the stability of synthesized PVA-SNT nanoparticles. The synthesized nanoparticles were immersed in PBS, FBS, and SBF solution for 24 h. The study confirms that PVA-SNT nanoparticles shows high stability in different solvent conditions. After incubation the hydrodynamic size distributions were studied which reveals 63.79 ± 3.35 nm for PBS, 57.25 ± 5.71 nm for SBF, and 59.4 ± 6.18 nm for FBS immersion respectively (Fig. 2a–c). UV–vis–NIR spectra of the PVA-SNT solution before and immediately after PTT treatment as well as

3 months after the treatment revealed stability without any significant changes in absorption spectra (Fig. 2d).

Measurement of the photothermal performance of PVA-SNT

Different concentrations (20, 60, 100, and 140 µg·mL^{-1}) of the synthesized PVA-SNT nanoparticles were placed in a 12-well cell culture plate. For photothermal therapy (PTT), a 808 nm laser was used at an optical density of 0.5, 1.0, 1.5, and 2.0 W·cm^{-2} for 20 min. Due to photothermal effects, the nanoparticle solution started heating up and the resulted temperature increase was recorded by an IR thermal camera (Fig. 2e). The PVA-SNT photothermal conversion efficiency ($\eta \approx 30.44\%$) was calculated following the procedure detailed in the Supporting Information (see Table S3, Fig. S3, Supporting Information) [52,53].

The optical properties of the different concentrations (20, 60, 100, and 140 µg·mL^{-1}) PVA-SNT solution were characterized by UV–vis spectroscopy which reveals strong NIR absorption (Fig. 1c). PVA-SNT solutions with different concentrations (20, 60, 100, and 140 µg·mL^{-1}) were added in a 12-well plate and exposed 1200 s to a 808 nm laser source at an optical power density of 0.5, 1.0, 1.5, and 2.0 W·cm^{-2} (Fig. 2f), respectively. Due to the photothermal effects the temperature elevation in these solutions reached 26.1, 33.4, 45.6, 54.1, and 56.4 °C, respectively, after 11 min of exposure at 1.0 W·cm^{-2} (Fig. 2g). The temperature of
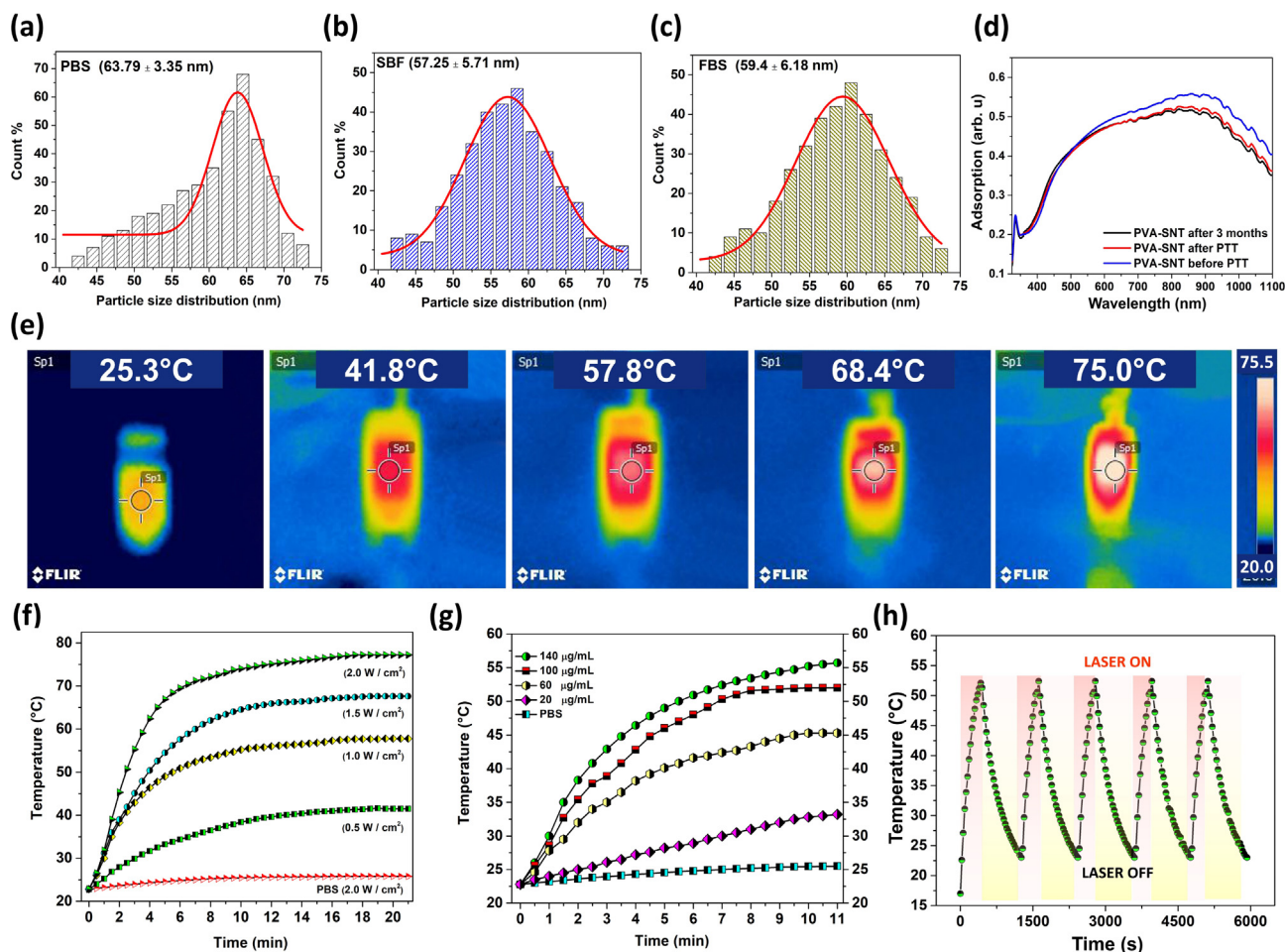

Fig. 2. (a) Biostability determination by hydrodynamic size distribution of PVA-SNT in different solvent (a) PBS, (b) SBF, (c) FBS solution. (d) Stability determination by UV–vis–NIR spectra of the PVA-SNT solution before and immediately after PTT treatment as well as 3 months after the treatment. (e) IR thermal imaging of 140 µg·mL^{-1} PVA-SNT nanoparticles exposed to 2.0 W·cm^{-2} 808 nm laser. (f) Temperature evolution of the 140 µg·mL^{-1} PVA-SNT solutions exposed for 20 min to a 808 nm laser source at four different optical power densities (0.5, 1.0, 1.5, and 2.0 W·cm^{-2}). (g) Temperature evolution of aqueous PVA-SNT with different concentrations exposed for 11 min to a 808 nm laser source at an optical power density of 1.0 W·cm^{-2}. (h) Temperature profile of the 140 µg·mL^{-1} PVA-SNT solution for five on/off cycles.

the 140 μg·mL^{-1} PVA-SNT solution increased to 41.8, 55.2, 67.6, and 77.4 °C after 1200 s of continuous irradiation at 2.0, 1.5, 1.0, and 0.5 W·cm^{-2}, respectively. The IR thermal imaging of 140 μg·mL^{-1} PVA-SNT nanoparticles exposed to 2.0 W·cm^{-2} 808 nm laser revealed a temperature elevation up to 75 °C (Fig. 2e). The temperature profile of the 140 μg·mL^{-1} PVA-SNT solution revealed a very stable performance during five on/off cycles (Fig. 2h).

These temperatures are therefore sufficient for in vivo cancer treatment since the optimal hyperthermia temperature is in the range 42–47 °C [54]. As a comparison, the control PBS sample (without nanoparticles) reaches a temperature of only 26.1 °C. The photothermal performance of the PVA-SNT solutions was well correlated with IR thermal images. At the end of the laser irradiation, the PVA-SNT nanoparticles were further characterized by UV–vis spectroscopy and FE-TEM (Fig. 2d and Supporting Information Fig. S4).

Theoretical analysis of the optical and photothermal properties of SNT

We performed electrodynamic simulations using the finite-difference time-domain method (FDTD, Ansys-Lumerical) [55] to calculate the absorption cross-section of randomly and uniformly distributed and randomly oriented SNT (5 nm thickness), silver hexagonal nanoplates (NH, 5 nm in thickness), and silver nanospheres (NS). The dielectric permittivity tabulated by Palik has been used for silver [56]. We used Gaussian size distributions and relative concentrations based on the experimental size distribution histograms and TEM images (Fig. 3a-c). The average size (measured as the radius of their circumcircle), standard deviation (σ), and the number of nanoparticles in the distribution are shown in Table 1. The relative concentration, defined as n_{part} is equal to the total count of a particle type divided by the total count of SNT in the histograms, that is, $n_{SNT} = 1$, $n_{NH} = 0.4$, and $n_{NS} = 0.7$. We used a cubic simulation region of $1.5 \times 1.5 \times 1.5$ μm^3
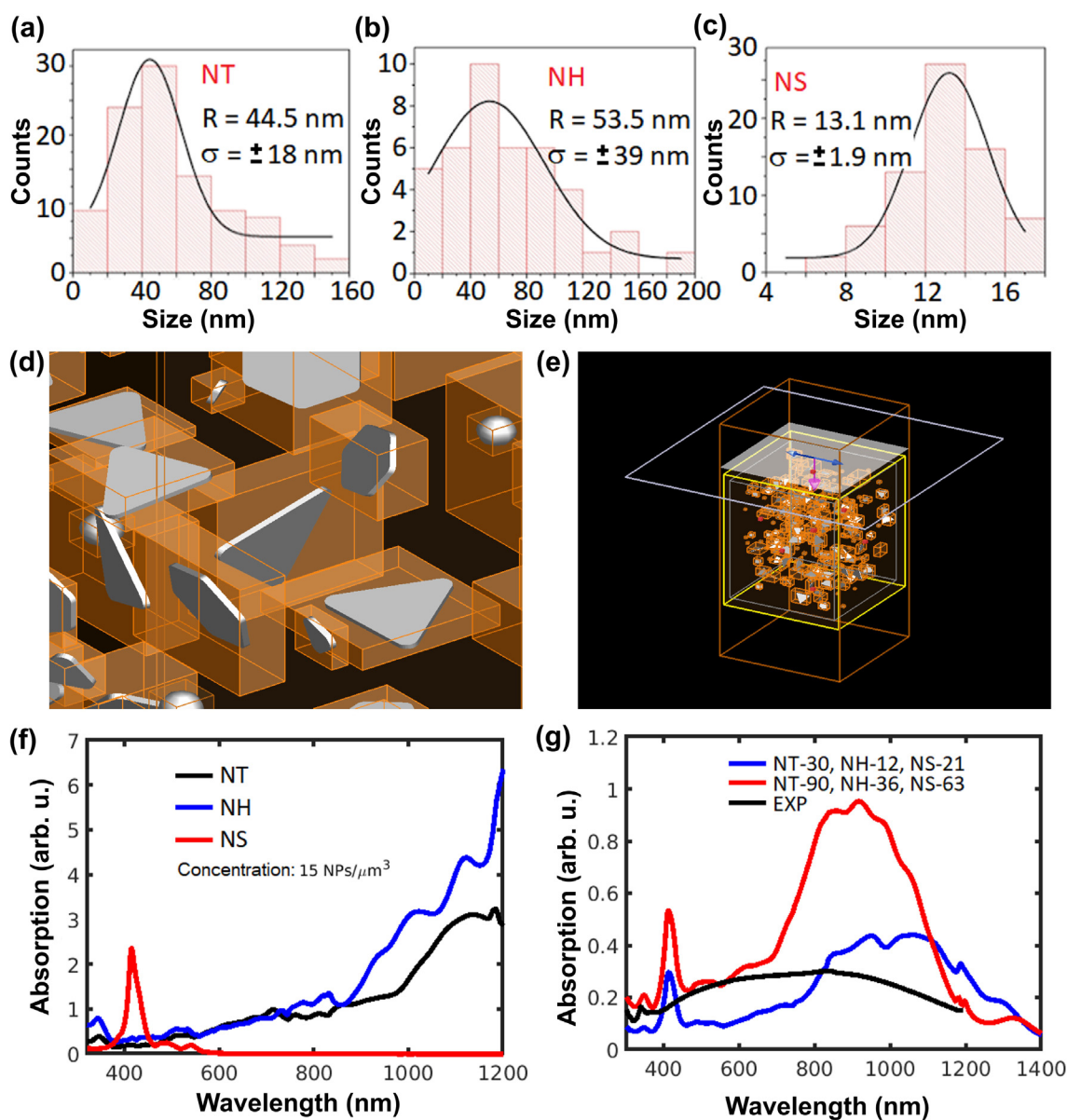

Fig. 3. Experimental size distributions of silver (a) NT, (b) NH, (c) NS used in the FDTD simulations. (d) Model of a distribution of silver NT, NH, and NS. (e) Simulation model used to calculate the absorption spectra. (f) Calculated absorption spectra associated with each type of nanoparticle in the same concentrations 15 NPs μm^{-3}: NT (black), NH (blue), and NS (red). (g) Absorption spectra of the combination of the three nanoparticles (NT, NH, and NS) in concentrations of 30, 12, and 21 NPs μm^{-3}, respectively (blue), and 90, 36, and 63 NPs μm^{-3} (red). The experimental absorption spectrum (black) is showed for comparison.

composed of water (refractive index n = 1.33) where the boundary conditions are periodic in the x- and y-directions and a perfect matched layer in the z-direction in order to model an infinite colloidal medium. The incident optical planewave was considered propagating in the *z*-direction and polarized in the *x*-direction (Fig. 3d, e).

First, we performed electrodynamic simulations to obtain the absorption spectra of each individual nanoparticle ensembles (NT, NH, and NS) with the same concentrations (15 NPs μm^{-3}). The calculated absorption spectra (Fig. 3f) show that the NT and NH exhibit a wide band in the NIR region while the NS exhibits only a dipolar plasmon mode at 413 nm. Then, two absorption spectra were calculated for a distribution composed of a mixture of the three nanoparticles using the two concentrations specified in Table 1 (n_{part}). The results are presented in Fig. 3g along with the experimentally measured absorption spectrum. At low NP concentration (blue spectrum), we note that a broad absorption band appears in the wavelength range 800–1200 nm due to the plas-

monic interaction between the NTs and the NHs, while the peak corresponding to the LSPR of the Ag NS remains at 413 nm (Fig. 3f,g). Increasing the concentrations three-fold (red spectrum) results in a blue-shift of the NIR broad band to 700–1100 nm due to the increasing near-field interaction between the nanoparticles. Further increase of the concentration leads to further broadening of the band, similar to the experimental spectrum. It is important to notice that for solutions with large nanoparticle concentrations (experimental conditions), the broad absorption band is centered around 800 nm, thus justifying the use of the 808-nm laser as optical source.

We performed a polarization dependence calculation of the absorption spectra of a single SNT with a size of 44.5 nm (mean experimental size, Fig. 3a) for six different optical excitation polarizations (Fig. 4a). All the calculated spectra show the same absorption peaks, related to different order multipolar modes at 910, 580, 525, and 475 nm, except the spectra calculated for a polarization along the *z*-direction (orange and magenta, Fig. 4a). For such trans-
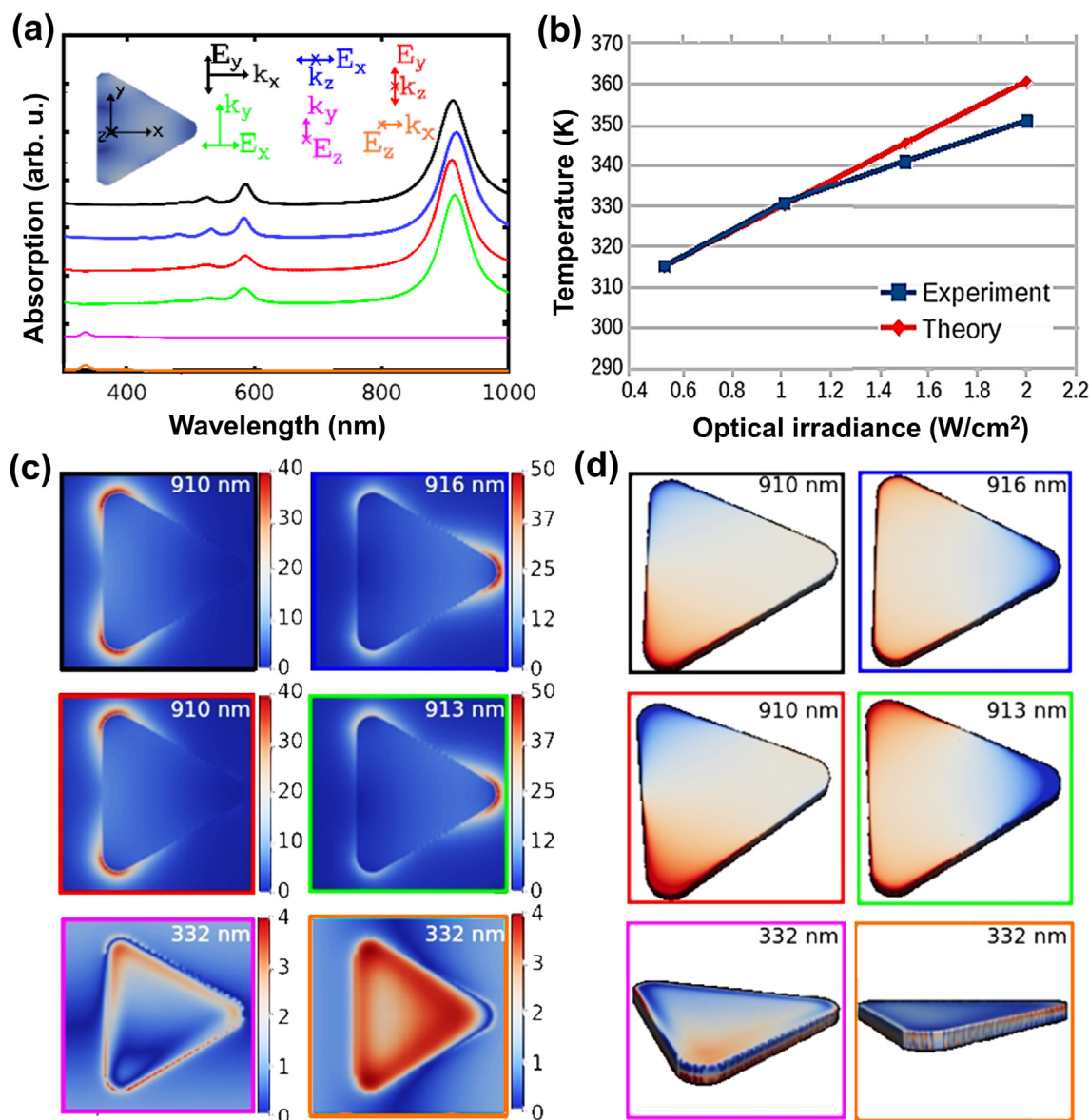
Fig. 4. (a) Absorption spectra of a SNT (44.5 nm of circumcircle radius) in water calculated for six different polarizations and propagation directions of the optical excitation. (b) Theoretical maximum temperature generated by the single SNT (red) and experimental temperature (blue). (c) Near electric field distributions in the (*x*, *y*)-plane and (d) surface charge density distributions of a SNT excited at the maximum absorption wavelength and for each of the six incident polarizations (color-coded with the spectra in (a)).

verse polarization, the spectra exhibit only one peak (332 nm) related to the out-of-plane dipole plasmon oscillation, which appears at ~340 nm in the experimental spectrum (Fig. 3f). The maximum absorption occurs at 910 nm, at which a high enhancement of the near electric field (NEF) is expected.

The main plasmon mode observed at 910 nm for SNT spectrally shifts to 940 nm for the PVA-SNT due to the presence of the PVA coating (see Fig. S5, Supporting Information). The presence of the thin PVA shell does not change the photothermal behavior of the nanoparticle because PVA has a molar heat capacity similar to that of water ($c_{p,m}$ = 75.38 J·mol^{-1}·K^{-1} for water and c_p = 61.5 J·mol^{-1}·K^{-1} for PVA). Therefore, the PVA coating does not induce any thermal shielding effect; hence, we consider that the photothermal analysis of SNT is sufficient for our analysis of PVA-SNT.

Near electric field distributions have been calculated for the 44.5 nm SNT under the six incident polarizations and at the maximum absorption wavelength (Fig. 4a). We can see that the NEF hotspots are located where there is a strong localization of the conduction electron density (Fig. 4c), *i.e.*, at some of the SNT vertices. The time-varying electric field distribution is shown in a supporting movie file (Mov-1). The NEF enhancement is very small (3-fold) for transverse polarizations (orange and magenta, Fig. 4a) due to the low localization of the out-of-plane plasmon mode, as compared to the 50-fold enhancement obtained for in-plane polarizations. The NEF for the other absorption bands show enhancements going from 10 to 25-fold (not shown here). These results are consistent with previous works on SNT [46]. Spatial distributions of the charge density were calculated in order to determine the modes of the plasmon resonances. From Fig. 4d, we can see a dipolar behavior of the plasmon mode for all the incident polarizations. The relative independence of the absorption spectrum and charge distribution on the in-plane polarization clearly highlights the in-plane optical isotropy of the SNT which exhibits its maximum absorption at 910–916 nm.

Finally, we have calculated the photothermal properties of a 44.5 nm SNT through a heat transfer simulation (using finite element method) [57]. In order to estimate the plasmonic heating of the SNT, we begin by finding the absorption cross-section (σ_{abs}) of the nanoparticle using an electrodynamic simulation (via FDTD method) to calculate the heat power defined by:

$$Q = \sigma_{abs} I \tag{1}$$

where I is the irradiance of the optical excitation (power per unit surface). Q acts as a heat source which induces an increase in the local temperature [58]:

$$\Delta T = \frac{Q}{4\pi \kappa_0 a_{SNT} + r} \tag{2}$$

where r is the distance from the metal surface, a_{SNT} is the SNT size, and κ_0 is the thermal conductivity of the surrounding medium. Though this model gives us a good approximation, it is better to solve the heat transfer equation using FEM to represents a heat source coming from the dissipation of the optical energy via the Joule effect, represented as:

$$\rho(\mathbf{r}) c_p(\mathbf{r}) \frac{\partial T(\mathbf{r}, t)}{\partial t} - \nabla[\kappa(\mathbf{r}) \nabla T(\mathbf{r}, t)] = -q(\mathbf{r}) \tag{3}$$

where ρ represents the mass density, c_p denotes the specific heat capacity, and κ represents the thermal conductivity. The function $q(\mathbf{r})$ is the applied heat energy transfer rate inside the SNT such that $Q = \int_V q(\mathbf{r}) d^3 r$, where the integral runs over the SNT volume V.

It is usually very fast to reach the local steady-state temperature when working with nanoscale systems. Typically, the duration of the transient regime is τ_{st} ~50–100 ns under continuous illumination and is not dependent on the temperature increase. As

mentioned before, we have begun to calculate the optical absorption power for optical irradiance values of 0.5, 1, 1.5, and 2 W·cm^{-2} using FDTD.

Fig. 4b shows the experimental photothermal steady-state temperatures (blue) at different laser power densities (0.5, 1.0, 1.5, and 2.0 W·cm^{-2}) under 808-nm laser irradiation and the theoretical maximum temperatures for the same power densities using an optical excitation at the maximum absorption wavelength. Theoretically, the temperature increases linearly as a function of the applied optical power, as shown in Equations (1) and (2). These results are in agreement with the computational work done by Manrique-Bedoya *et al.* [57] There is an excellent agreement between the temperatures predicted from the theory and the experimental measured temperatures (within 2% at high power density). The slight deviation from the theoretical model observed at high powers can be explained by the thermal energy lost in the environment (heat dissipation), water volatilization from the cells, and protein denaturation [59,60]. The multi-physics simulation approach based on plasmonic nanoparticles shape, size, concentration, and composition could be useful for the prediction of photothermal heat generation.

MTT assay for in vitro cytotoxicity study

The MTT assay of SNT nanoparticles revealed non-toxic property to the MDA-MB-231 cell line after 24 h incubation with different concentrations (Fig. 5a). The lowest concentration (20 µg·mL^{-1}) yielded more than 95% relative cell viability, while a higher concentration of 120 µg·mL^{-1} yielded a slightly higher toxicity with ~11% of dead cells. The largest concentration (140 µg·mL^{-1}) also yielded ~89% cell viability, which led us to conclude SNT nanoparticles exhibit very little toxic behavior up to this concentration. A similar study was performed with PVA-SNT nanoparticles, incubated with the same concentrations for 24 h, with the MDA-MB-231 cell line. The PVA-SNT nanoparticles show a higher level of cell viability (~87% for 100 µg·mL^{-1}) compared to the SNT nanoparticles. When the PVA-SNT concentration reaches 120 µg·mL^{-1}, little toxicity was observed (overall cell viability is approximately 95%). Finally, the highest concentration of 140 µg·mL^{-1} showed ~96% cell viability (Fig. 5b). PVA is a biopolymer which helps to protect the cell line from any toxic effect due to its stable polymeric coating which retards the ions released from the silver nanoparticles. Because this study was performed to determine the photothermal effects of metal nanoparticles on MDA-MB-231 cell lines, SNT nanoparticles incubated with MDA-MB-231 cell lines were exposed to 1.0 W·cm^{-2} laser irradiation (Fig. 5c). Compared to the control column, different concentrations of SNT nanoparticles showed toxic effects when exposed to laser light. The toxicity level of laser-irradiated nanoparticles increased as the concentration of nanoparticles increased. With 1.0 W. cm^{-2} laser irradiation, a low concentration nanoparticle dose (20 µg·mL^{-1}) led to ~88% of cell viability, while increasing the concentration up to 140 µg·mL^{-1} the cell viability drastically reduced to ~2%. Similar fatal effect was observed when MDA-MB-231 cell lines were treated with laser-irradiated PVA-SNT nanoparticles (Fig. 5d). When the MDA-MB-231 cell lines were treated with 120 and 140 µg·mL^{-1} of PVA-SNT nanoparticles (with 1.0 W·cm^{-2} laser irradiation), the cell viability drastically changes to less than ~10% and ~5%, respectively. With laser irradiation, the non-toxic PVA-SNT nanoparticles also generate sufficient heat to kill the cancer cells. The synergistic effect of heat generation with different PVA-SNT concentrations on variable laser power density is shown in Fig. 5e. From this study we conclude that higher concentrations and high laser power densities are lethal to cell lines. To get the optimal effect on target cancer cells we chose a PVA-SNT concen-
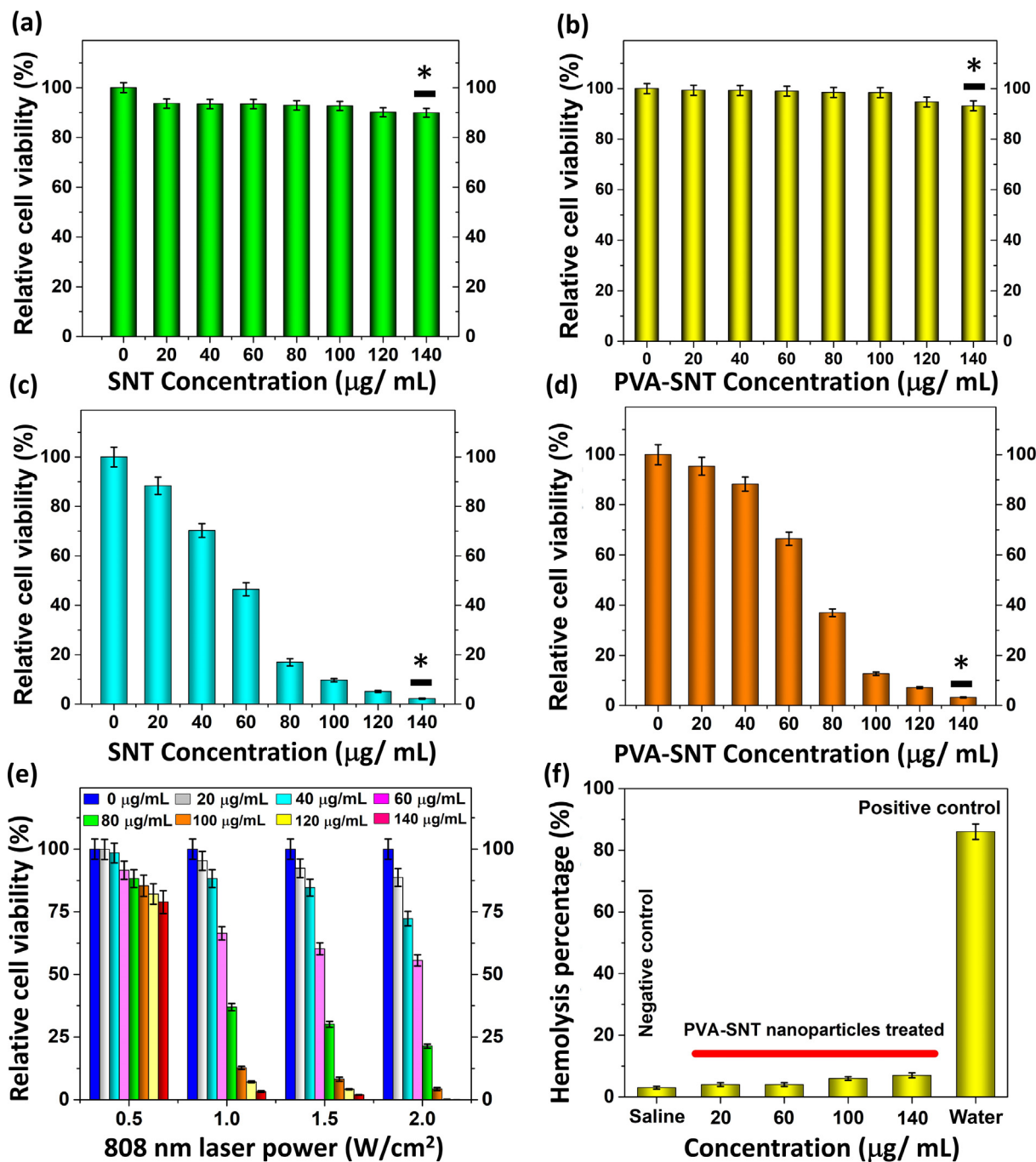
Fig. 5. Cell viability of MDA-MB-231 cells after 24 h incubation with different concentrations of (a) SNT. (b) PVA-SNT. (c) SNT and 808 nm laser (1.0 W·cm^{-2}) for 7 min. (d) PVA-SNT and 808 nm laser (1.0 W·cm^{-2}) for 7 min. (e) PVA-SNT nanoparticles with different optical power density (0.5, 1.0, 1.5, and 2.0 W·cm^{-2}). Data were expressed as mean ± S.D. (n = 5, *significant p < 0.05 vs control as statistically significant). (f) Hemolysis study of PVA-SNT nanoparticles.

tration of 140 μg·mL^{-1} with a laser power density of 1.0 W·cm^{-2} as the optimal therapeutic dose.

Hemolysis study

To perform the hemocompatibility assay blood samples were aspirated from nude mice with further heparin-stabilization. The collected red blood cells (RBCs) were mixed with 10 × PBS. The RBCs suspension (400 μL) was treated with PVA-SNT nanoparticles in 1.1 mL of PBS at different concentrations of 20, 60, 100, and 140, μg·mL^{-1} with distilled water as positive and medical saline solution as negative control, respectively. After mixing well all the

solutions were incubated at 37 °C for 4 h and finally centrifuged at 5200 rpm for 5 min. The absorbance of each sample was quantified on a Tecan Infinite F50 microplate reader at 541 nm wavelength. The hemolysis of RBCs for all the samples was calculated using the following equation:

$$Hemolysis(\%) = \frac{Abs_{Sample} - Abs_{Negative\ control}}{Abs_{Positive\ control} - Abs_{Negative\ control}}$$

To study the in vivo cancer therapeutic efficacy, PVA-SNT nanoparticles were injected intratumor region. Thus, the blood compatibility of the injected nanoparticle is essentially important to investigate. As depicted in Fig. 5f, PVA-SNT showed hemolytic

activities of 6.18 ± 0.17% at a high concentration of 140 µg·mL^{-1}, showing the excellent blood compatibility of the synthesized nanomaterials (see Fig. S6, Supporting Information).

Fluorescent staining for cell viability study

MDA-MB-231 cell lines were incubated with 140 µg·mL^{-1} solutions of SNT and PVA-SNT nanoparticles (Fig. 6). Only MDA-MB-231 cell lines were studied as control, without any nanoparticles and without any laser irradiation (Fig. 6a & 6e). Cells were treated in two different groups, stained with AO/PI and Hoechst 33342/ PI. The propidium iodide (PI) fluorescence, only permeable to dead cells and during fluorescence excitation, yields the emission of a red signal from dead cells only. When studied under fluorescence microscope, most of the cells are emitting green fluorescent light (AO/PI treatment), which reveals the healthy state of the cells (Fig. 6a-c). For Hoechst 33342/ PI stained cells emitted mostly blue fluorescent showing the cellular viability status (Fig. 6 e-g). Hoechst stains are permeable to live cell nucleus which emits blue fluorescence when combined with dsDNA. Only laser irradiated PVA-SNT-incubated cells showed a significant amount of red fluorescence, which indicates the presence of dead cells (Fig. 6d & 6 h). Biological-TEM study reveals the internalization of PVA-SNT nanoparticles inside the cellular environment (see Fig. S7, Supporting Information). From the MTT study we observed toxic effects from high SNT concentration. Fluorescence measurements of the PVA-SNT-treated MDA-MB-231 cell line revealed a considerable number of live cells with acridine orange's (AO) green emission (Fig. 6b) and Hoechst 33,342 emits blue fluorescent (Fig. 6f). This result is well correlated with the MTT assay of the PVA-SNT-incubated MDA-MB-231 cell line. The non-toxic PVA-SNT turned to lethal toxic material when irradiated with an 808 nm, 1.0 W·cm^{-2} laser at a concentration of 140 µg·mL^{-1} (Fig. 6d & 6 h). The study revealed more than 99% cell death with all red fluorescence from the dead cells over a microscopic region.
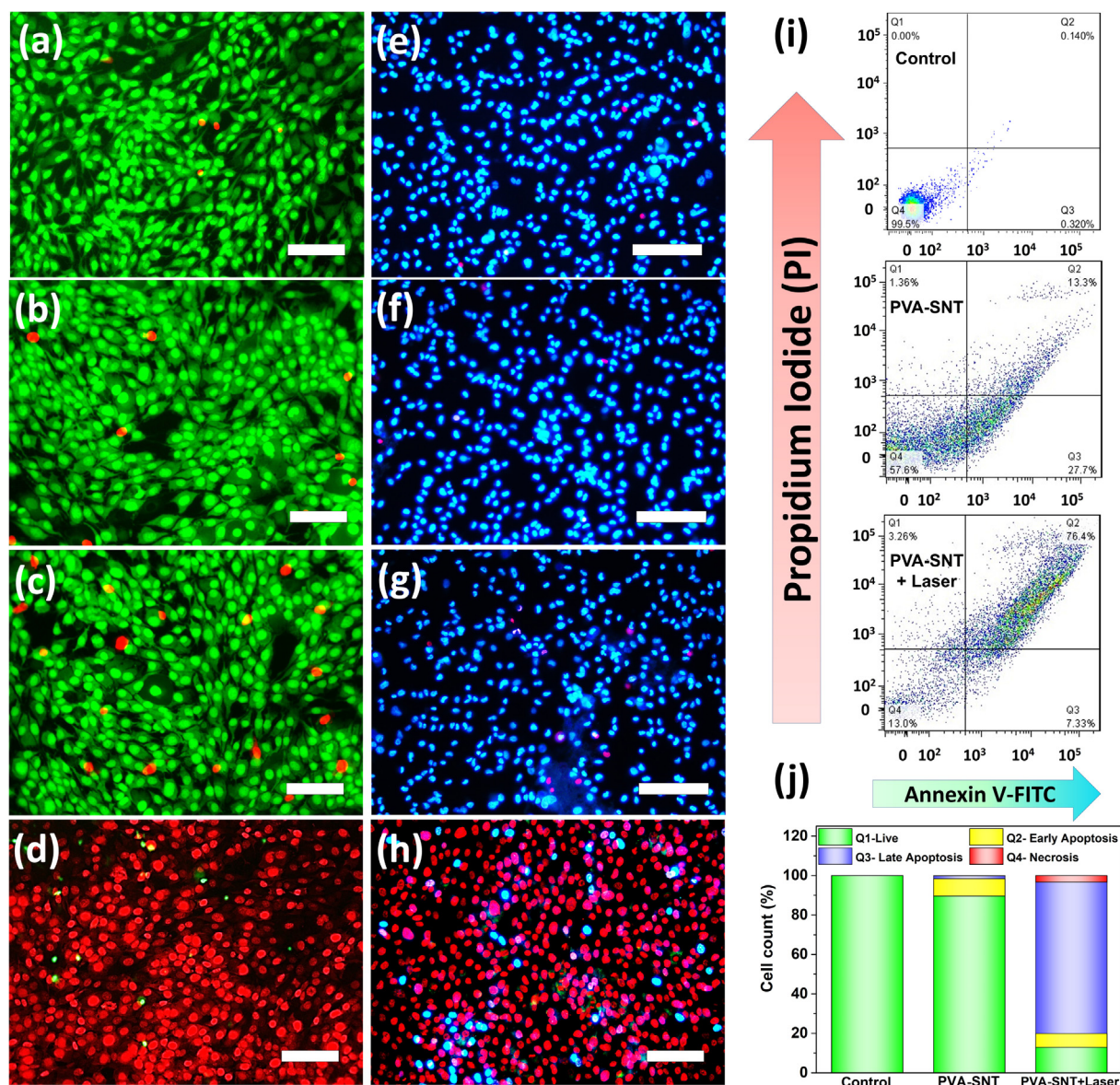
Fig. 6. AO/PI live and dead cell fluorescent staining of MDA-MB-231 breast cancer cell line treated with (a & e) Control (without any nanoparticles or laser irradiation). (b & f) SNT without laser irradiation. (c & g) PVA-SNT without laser irradiation. (d & h) PVA-SNT with 808 nm laser irradiation. [Scale bar = 25 µm for Fig. 6a, b, c, d, h and Scale bar = 50 µm for Fig. 6 e, f, g] (i & j) Flow cytometry analysis of MDA-MB-231 cells apoptosis induced by PVA-SNT, with and without laser irradiation using the PI/Annexin V staining.

The flow cytometry was performed with PVA-SNT nanoparticle treated with the MDA-MB-231 cell line with and without 1.0 W·cm^{-2} laser irradiation (Fig. 6i & 6j). Control cells were studied in absence of nanoparticles and laser irradiation. The flow cytometry study revealed approximately 99.9% cells in healthy condition for the control group with ∼0.08% in the early and ∼0.05% in late apoptosis stage (no cells were found in necrosis stage). For PVA-SNT treated cells without any laser exposure, we observed ∼89.6% cells in healthy condition with ∼8.77% in early 1.38% in late apoptosis phase. Very little amount (∼0.2%) was observed in necrosis stage. However, a drastic change in cell viability was observed for PVA-SNT and laser-irradiated cells. For the treated cells ∼12.9% were found to be healthy with ∼6.91% in early and ∼76.8% in late apoptosis phase. Additionally, ∼3.39% of the cells showed necrosis due to the photothermal effects.

Photoacoustic imaging (PAI)

The in vitro PAI result reveals the absence of signal from the control tube whereas, PVA-SNT loaded tubes generate low to high signal according to the increased nanoparticle concentration (Fig. S8, Supporting Information). A detailed analysis of the signal plotted as the gray value histogram, provides a different photoacoustic signal which generates due to the presence of different nanoparticles concentrations (Fig. S8, Supporting Information).

Furthermore, this experimental study also extends to in vivo PAI. The mouse models with MDA-MB-231 tumor were injected with 100 μL of PVA-SNT (140 μg·mL^{-1}) through intra-tumoral injection. Fig. 7a shows *In vivo* 3D PAI of tumor tissues in nude mice (i) before, (ii) after injection of PVA-SNT performed using a PAM system with 532–1000 nm, (iii) after injection with 625–1000 nm filters, and (iv) the merging of figure (ii) & (iii).

To study the nanoparticles effects, we designed the experimental study pre and post injection with two filter modes, which were chosen to visualize (i) the blood vessel (532–1000 nm) and (ii) the nanoparticles (625–1000 nm). To conduct the experimental study, we first scanned an entire tumor region in pre-injection state applying the two different filters. In case of the 532 nm filter, we were only able to observe the blood vessel of the mouse in the tumor region, due to the absorbance of blood hemoglobin at 532 nm (Fig. 7b). On the other hand, the 625 nm filter blocked the entire absorbance signal from the blood hemoglobin. After the injection of 140 μg·mL^{-1} of PVA-SNT nanoparticles, a bright tumor region was observed along with the blood vessels. To confirm the exact location and size of the tumor we made another scan with the 625 nm filter, which also precisely provided the tumor shape and size. This PAI technique is extremely helpful to treat tumors while determining the exact location for PTT. The reconstructions of 3D views from the experimental PAM data are attached as supporting movie files (Mov-2, Mov-3, Mov-4, and Mov-5).
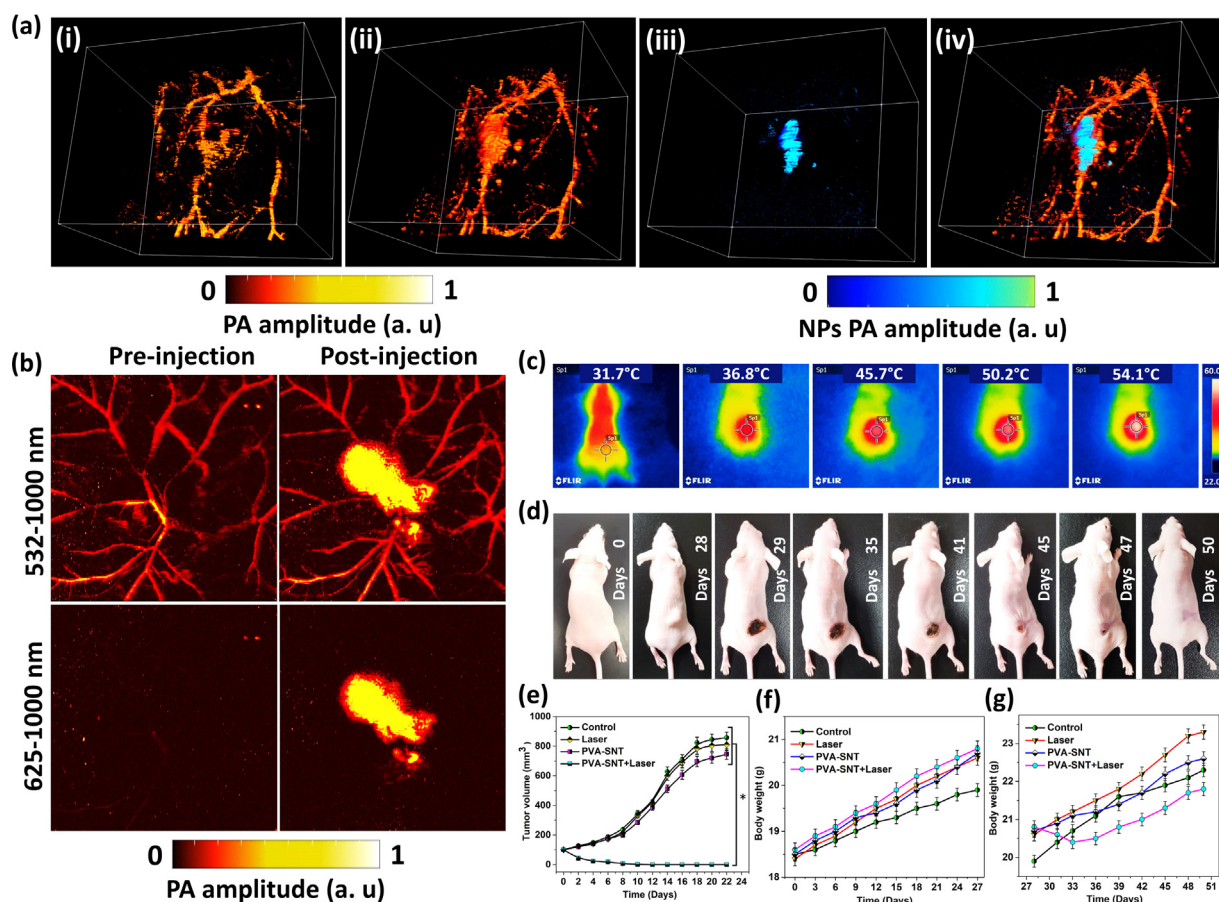

Fig. 7. (a) *In vivo* 3D PAI of tumor tissues in MDA-MB-231 tumor-bearing nude mice (i) before and (ii) after injection of PVA-SNT performed using a PAM system with 532–1000 nm and (iii) after injection with 625–1000 nm filters (iv) the merging of figure (ii) & (iii) [experimental PAM data are attached as supporting movie files (Mov-2, Mov-3, Mov-4, and Mov-5)] (b) *In vivo* 2D PAI of tumor tissues in MDA-MB-231 tumor-bearing nude mice before and after injection of PVA-SNT performed using a PAM system with 532–1000 nm and 625–1000 nm filters. (b) (c) IR thermal image of the mouse during photothermal treatment. The laser irradiated for 7 min from 808 nm laser source at an optical power density of 1.0 W·cm^{-2}. (d) Representative photographs of MDA-MB-231 tumor-bearing nude mice from day 0, tumor induced (day 28), photothermal treatment initiated (day 29), and up to complete healing (day 50). (e) Tumor volume of various groups after PTT treatments. Data were expressed as mean ± S.D. (*n* = 3, *significant *p* < 0.05) (f) Body weight of the mice before PTT treatments. (g) Body weight of the mice after PTT treatments.

In vivo photothermal therapy

The experimental mice were divided into four groups, from which groups II and IV underwent laser treatment. Additionally, the mice from group II were not injected with any nanoparticles. From the in vitro study it was confirmed that no heat generation occurs in absence of nanoparticles, thus PTT was not effective for group II. The tumors were irradiated with a 1.0 W·cm^{-2} laser (808 nm) for 7 min. The initial experimental study started at room temperature 25 ± 2 °C, whereas, the mouse's initial body temperature was 31.2 ± 1.6 °C. After irradiation by a 1.0 W·cm-2 laser (808 nm) for 7 min, the animals from group II showed a maximum temperature increase of 1.9 °C, which resulted a final body temperature of 33.1 ± 0.6 °C. Since there were no nanoparticles inside the target tumor region, the laser dosage alone could not elevate the temperature [61]. Group IV animals were intratumorally injected with 100 μL of 140 μg·mL-1 PVA-SNT solution and exposed under 1.0 W·cm-2 laser (808 nm) for 7 min. The IR thermal images in Fig. 7c show the mouse body temperature increases from 31.7 to 54.1 °C during the photothermal treatment. After the photothermal treatment, again the tumor region recorded a temperature of 33.4 °C, which was close to the mouse's normal body temperature.

The temperature elevation in the tumor region was sufficient to treat the tumors in animal model. No animal died after the treatment, which confirms the safety aspects of this therapy. Additionally, there were no significant changes in the behavior or body weight of the mice resulting from the photothermal shock. Our study found no noticeable toxicity or lethal effect, which supports the conclusions from earlier reports [62]. All the mice were observed for an entire 4 weeks after treatment, until the complete healing of the photothermal effects (Fig. 7d).

After the MDA-MB-231 cell line injection inside mouse body it took 4 weeks to grow a workable tumor. The PTT treatment was started on the 29th day post tumor cell injection. The mice were taken at regular intervals for photography. Beside food and water, no medication was provided to the mice. With the progress of time the mouse affected tumor region was healed and no further tumor growth was observed. The tumor volume and body weight were regularly recorded for all the animals (Fig. 7e-g). The body weight of all the experimental group mice was recorded at regular time intervals. Up to 28 days after tumor induction, all the groups showed regular weight gain. To the exception of mice treated with the nanoparticles and laser (group IV), which show an effective tumor inhibition progress with no further recurrence, all remain-
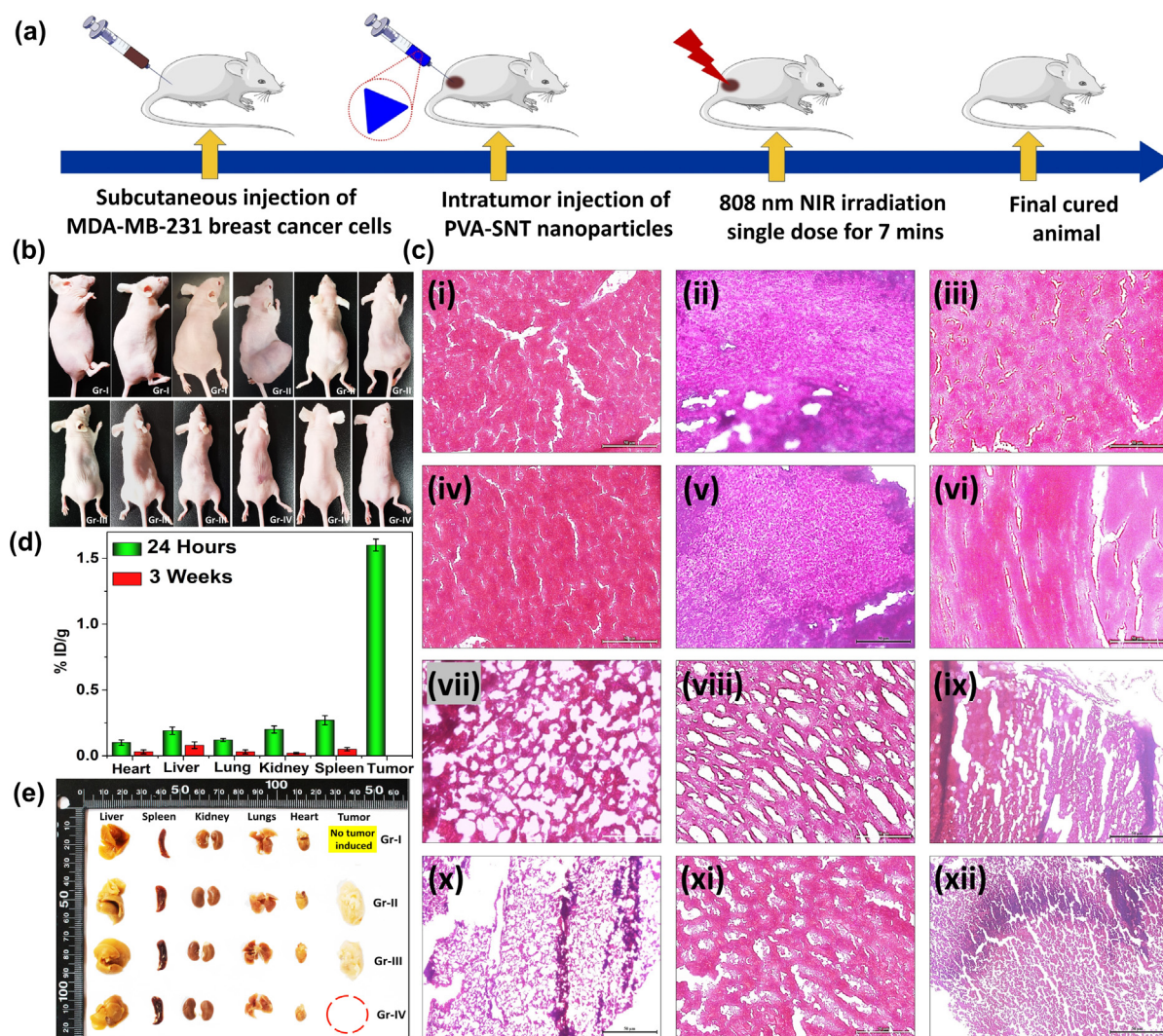
Fig. 8. (a) Schematics illustration of in vivo experimental progress (b) Animals used in the in vivo study (all groups) after the photothermal treatment. (c) H&E stained images of organs [(i) control (iv) treated liver, (ii) control (v) treated spleen, (iii) control (vi) treated kidney, (vii) control (x) treated lungs, (viii) control (xi) treated heart, (ix and xii) tumor after various treatments (20× magnification; Scale bars: 50 μm)]. (d) Biodistribution of silver in the organs (heart, liver, lungs, kidney, and spleen) and tumor of the mice treated with PVA-SNT for 24 h and 4 weeks post treatment. (e) Organs (heart, liver, lungs, kidney, and spleen) and tumor recovered from post treatment mice model.

ing tumors grew larger (Fig. 7e and Fig. S9, Supporting Information). Contrary to the control group, tumor bearing mice gained more weight (Fig. 7f). After the photothermal treatment the group IV mice suddenly lost weight; and after a week of post photothermal therapy the group showed normal weight gain (Fig. 7g). These results confirm that PVA-SNT nanoparticles could be useful as theranostic material with both diagnostic and therapeutic properties.

Histological analysis

The in vivo experimental study was performed for 7 weeks, from tumor induction to photothermal treatment (Fig. 8a). All the mice were observed and taken care of for an entire 4 weeks post PTT treatment, until the complete healing (Fig. 8b). The histological analysis was performed after finishing the PTT study with post treatment observation. The major organs (liver, spleen, kidney lung, and heart) were collected and treated for H&E staining as discussed in the experimental section (Fig. 8c). The histological images of tissues are presented in Fig. 8c. The healthy tissues with no abnormal characteristics and lack of drastic body weight changes strongly supports the nontoxic behavior of the PVA-SNT therapeutics. While studying the histological section of the tumor tissues we observed some significant changes resulting from the PTT effects (Fig. 8c). The untreated tumors (groups I and II) show poorly differentiated cells with granulated deep stained nuclei, whereas PVA-SNT treated animals (group III) show moderate size tumors with deep stained cells and granulated nuclei. Finally, animals treated with PVA-SNT and laser irradiation (group IV) show no sign of tumors. While collecting the post-treatment surrounding tissues all healthy cells with prominent nucleus were observed; there was no sign of cancerous tissues observed in the treated animals of group IV. During the observation period, all the tumor volumes were measured at regular time intervals (Fig. 7g and Supporting Information).

Biodistribution of PVA-SNT nanoparticles

The size of the nanoparticles plays an important role during in vivo circulation. Less than ~8 nm nanoparticles undergo efficient urinary excretion due to the pore size limit of glomerular filtration in the kidneys [63]. Our synthesized PVA-SNT is 13–90 nm in size which is most likely to be cleared by hepatobiliary fecal elimination [64].

To analyze the accumulation of PVA-SNT in organs, randomly selected mice from treated groups were sacrificed at 24 h and 4-week time intervals. The organs were dissected and lysed with 8 h HNO_3 treatment. The silver concentration was quantified using inductively coupled plasma mass spectrometry (ICP-MS). The results show a high level of AgNPs at 24 h post tumor treatment (Fig. 8d). At 24 h, the calculated accumulated percentage of post injected dose per gram of tissue in tumor was about 2.1% $ID\cdot g^{-1}$. Although it was an intratumoral injection, the nanoparticles were able to mix with nearest blood flow and accumulate throughout the different organs inside body system. As a result, the spleen accumulated the highest amount (~0.27% $ID\cdot g^{-1}$ at 24 h and ~0.05% $ID\cdot g^{-1}$ after three weeks), whereas kidney, liver, lungs, and heart accumulated 0.2, 0.19, 0.12, and 0.1% $ID\cdot g^{-1}$, respectively, after 24 h post treatment. After 4 weeks, a biodistribution study revealed a significant clearance of the nanoparticles from the body system, with very negligible amounts: 0.05, 0.02, 0.08, 0.03, and 0.03% $ID\cdot g^{-1}$ for the spleen, kidney, liver, lungs, and heart, respectively. Due to this minute nanoparticle amount inside the organs, there were no toxic or lethal effects. The organs and the tumor were observed under an optical microscope to find any physiological and structural changes (Fig. 8e). No such abnormalities were observed in any of the organs; all the cross-sectional tis-

sues appeared with healthy morphologies. Additionally, no significant color change was observed; hence, the organs appeared to be normal for all the experimental groups (I-IV). The overall study concludes that the nanoparticles and their doses used here are nontoxic, nonlethal, and highly effective for photothermal cancer therapy.

Conclusion

Cancer management has been one of the biggest conundrums in the biomedical field. Photothermal therapy (PTT) now a day gain attention as an emerging alternative to chemotherapy and radiotherapy, which have associated to serious side-effects. Our study was designed in combination with computational simulations to estimate the plasmonic heat generation with a high accuracy and which could be reliably compared to experimental results. A drug-free PVA-SNT nanoparticle was synthesized and used as a theranostic probe, which proved its excellent contrast efficiency with enhanced photothermal activity against triple-negative breast cancer mouse model. After coating with PVA synthetic biopolymer, PVA-SNT nanoparticles showed excellent biosafety, biocompatibility, photostability, and broad near-infrared absorbance. The material of choice, silver, is much cheaper than gold and has a nearly equal efficiency with respect to plasmonic properties. The stability issue of silver was overcome by surface chemistry modification using PVA. The experimental study was performed in vitro and in vivo, and displayed a powerful anticancer efficiency with photoacoustic imaging guided photothermal treatment property. PTT relies on ablation agents capable of converting light into heat to kill the cancer cells without affecting normal cells due to their better heat tolerance ability. A well-studied standardized dose of 140 µg·mL^{-1} PVA-SNT nanoparticles with 1.0 W·cm^{-2} laser irradiation for 7 min proved to be an effective and optimized theranostic approach in terms of PAI guided treatment of triple negative breast cancer management. This proposed combined theoretical-experimental strategy may help researchers to better understand other nanoparticles in terms of plasmonic efficiency and usability, for future nano-biomedical research.

Compliance with Ethics Requirements

All Institutional and National Guidelines for the care and use of animals were followed.

Animal study Ethics statement:

All animal experiments involving animals were conducted according to the ethical policies and procedures approved by the Ethical Committee of Pukyong National University, Busan, (Approval no. PKNUIACUC-2019-05), and also followed the Animal Ethical Policies of the Republic of Korea.

CRediT authorship contribution statement

Sudip Mondal: Conceptualization, Investigation, Methodology, Validation, Writing – original draft. **José Luis Montaño-Priede:** Conceptualization, Investigation, Writing – review & editing. **Van Tu Nguyen:** Writing – review & editing. **Sumin Park:** Investigation, Methodology, Writing – review & editing. **Jaeyeop Choi:** Investigation, Writing – review & editing. **Vu Hoang Minh Doan:** Investigation, Writing – review & editing. **Thi Mai Thien Vo:** Investigation, Writing – review & editing. **Tan Hung Vo:** Writing – review & editing. **Nicolas Large:** Conceptualization, Investigation, Supervision, Funding acquisition, Writing – review & editing. **Chang-Seok Kim:** Conceptualization. **Junghwan Oh:** Conceptualization,

Methodology, Validation, Writing – review & editing, Funding acquisition, Supervision.

Declaration of Competing Interest

The authors declare that they have no known competing financial interests or personal relationships that could have appeared to influence the work reported in this paper.

Acknowledgements

Appendix A. Supplementary material

Supplementary data to this article can be found online at https://doi.org/10.1016/j.jare.2022.02.006.

References

[1] van der Meel R, Sulheim E, Shi Y, Kiessling F, Mulder WJ, Lammers T. Smart cancer nanomedicine. Nat Nanotechnol 2019;14(11):1007–17.

[2] Lim E-K, Kim T, Paik S, Haam S, Huh Y-M, Lee K. Nanomaterials for theranostics: recent advances and future challenges. Chem Rev 2015;115(1):327–94.

[3] Xu C, Feng Q, Yang H, Wang G, Huang L, Bai Q, et al. A Light-Triggered Mesenchymal Stem Cell Delivery System for Photoacoustic Imaging and Chemo-Photothermal Therapy of Triple Negative Breast Cancer. Adv Sci 2018;5(10):1800382.

[4] Huang X, El-Sayed MA. Gold nanoparticles: Optical properties and implementations in cancer diagnosis and photothermal therapy. J Adv Res 2010;1(1):13–28.

[5] Feng G, Zhang G-Q, Ding D. Design of superior phototheranostic agents guided by Jablonski diagrams. Chem Soc Rev 2020;49(22):8179–234.

[6] Chen Y, Jungsuwadee P, Vore M, Butterfield DA, St Clair DK. Collateral damage in cancer chemotherapy: oxidative stress in nontargeted tissues. Mol Interventions 2007;7(3):147.

[7] Chen J, Ning C, Zhou Z, Yu P, Zhu Y, Tan G, et al. Nanomaterials as photothermal therapeutic agents. Prog Mater Sci 2019;99:1–26.

[8] Huang X, Jain PK, El-Sayed IH, El-Sayed MA. Plasmonic photothermal therapy (PPTT) using gold nanoparticles. Lasers Med Sci 2008;23(3):217–28.

[9] Austin LA, Mackey MA, Dreaden EC, El-Sayed MA. The optical, photothermal, and facile surface chemical properties of gold and silver nanoparticles in biodiagnostics, therapy, and drug delivery. Arch Toxicol 2014;88(7):1391–417.

[10] Du R, Wang J, Wang Y, Hübner R, Fan X, Senkovska I, et al. Unveiling reductant chemistry in fabricating noble metal aerogels for superior oxygen evolution and ethanol oxidation. Nat Commun 2020;11(1):1–10.

[11] Hu R, Yong K-T, Roy I, Ding H, He S, Prasad PN. Metallic nanostructures as localized plasmon resonance enhanced scattering probes for multiplex dark-field targeted imaging of cancer cells. J Phys Chem C 2009;113(7):2676–84.

[12] Matschulat A, Drescher D, Kneipp J. Surface-enhanced Raman scattering hybrid nanoprobe multiplexing and imaging in biological systems. ACS Nano 2010;4(6):3259–69.

[13] Boca-Farcau S, Potara M, Simon T, Juhem A, Baldeck P, Astilean S. Folic acid-conjugated, SERS-labeled silver nanotriangles for multimodal detection and targeted photothermal treatment on human ovarian cancer cells. Mol Pharm 2014;11(2):391–9.

[14] Zhao Z, Chen C, Wu W, Wang F, Du L, Zhang X, et al. Highly efficient photothermal nanoagent achieved by harvesting energy via excited-state intramolecular motion within nanoparticles. Nat Commun 2019;10(1):1–11.

[15] Boca SC, Potara M, Gabudean A-M, Juhem A, Baldeck PL, Astilean S. Chitosan-coated triangular silver nanoparticles as a novel class of biocompatible, highly effective photothermal transducers for in vitro cancer cell therapy. Cancer Lett 2011;311(2):131–40.

[16] Pastoriza-Santos I, Liz-Marzán LM. Colloidal silver nanoplates. State of the art and future challenges. J Mater Chem 2008;18(15):1724–37.

[17] Wei B, Dong F, Yang W, Luo C, Dong Q, Zhou Z, et al. Synthesis of carbon-dots@SiO2@ TiO2 nanoplatform for photothermal imaging induced multimodal synergistic antitumor. J Adv Res 2020;23:13–23.

[18] Cao YC, Jin R, Mirkin CA. Nanoparticles with Raman spectroscopic fingerprints for DNA and RNA detection. Science 2002;297(5586):1536–40.

[19] Zhang Q, Large N, Wang H. Gold nanoparticles with tipped surface structures as substrates for single-particle surface-enhanced Raman spectroscopy: concave nanocubes, nanotrisoctahedra, and nanostars. ACS Appl Mater Interfaces 2014;6(19):17255–67.

[20] Gao C, Lu Z, Liu Y, Zhang Q, Chi M, Cheng Q, et al. Highly stable silver nanoplates for surface plasmon resonance biosensing. Angew Chem Int Ed 2012;51(23):5629–33.

[21] Chen C, Ou H, Liu R, Ding D. Regulating the photophysical property of organic/polymer optical agents for promoted cancer phototheranostics. Adv Mater 2020;32(3):1806331.

[22] Mondal S, Reyes MEDA, Pal U. Plasmon induced enhanced photocatalytic activity of gold loaded hydroxyapatite nanoparticles for methylene blue degradation under visible light. RSC Adv 2017;7(14):8633–45.

[23] Jing H, Zhang Q, Large N, Yu C, Blom DA, Nordlander P, et al. Tunable plasmonic nanoparticles with catalytically active high-index facets. Nano Lett 2014;14(6):3674–82.

[24] Jaque D, Maestro LM, del Rosal B, Haro-Gonzalez P, Benayas A, Plaza J, et al. Nanoparticles for photothermal therapies. Nanoscale 2014;6(16):9494–530.

[25] Rycenga M, Cobley CM, Zeng J, Li W, Moran CH, Zhang Q, et al. Controlling the synthesis and assembly of silver nanostructures for plasmonic applications. Chem Rev 2011;111(6):3669–712.

[26] Wiley B, Sun Y, Xia Y. Synthesis of silver nanostructures with controlled shapes and properties. Acc Chem Res 2007;40(10):1067–76.

[27] Lal S, Link S, Halas NJ. Nano-optics from sensing to waveguiding. Nanosci Technol: Collect Rev Nat J, World Scientific 2010:213–20.

[28] Le Ru E, Etchegoin P. Principles of Surface-Enhanced Raman Spectroscopy: and related plasmonic effects. Elsevier; 2008.

[29] Perner M, Bost P, Lemmer U, Von Plessen G, Feldmann J, Becker U, et al. Optically induced damping of the surface plasmon resonance in gold colloids. Phys Rev Lett 1997;78(11):2192.

[30] Wang H, Tam F, Grady NK, Halas NJ. Cu nanoshells: effects of interband transitions on the nanoparticle plasmon resonance. J Phys Chem B 2005;109(39):18218–22.

[31] Xia Y, Xiong Y, Lim B, Skrabalak SE. Shape-controlled synthesis of metal nanocrystals: simple chemistry meets complex physics? Angew Chem Int Ed 2009;48(1):60–103.

[32] Fauss EK. Risk Analysis of Nanotechnology through Expert Elicitation: A Silver Nanotechnology Case Study. University of Virginia; 2008.

[33] Sokolov K, Follen M, Aaron J, Pavlova I, Malpica A, Lotan R, et al. Real-time vital optical imaging of precancer using anti-epidermal growth factor receptor antibodies conjugated to gold nanoparticles. Cancer Res 2003;63(9):1999–2004.

[34] Kumar A, Mazinder Boruah B, Liang X-J. Gold nanoparticles: promising nanomaterials for the diagnosis of cancer and HIV/AIDS. J Nanomater 2011 (2011)..

[35] Borghei Y-S, Hosseinkhani S, Ganjali MR. "Plasmonic Nanomaterials": An emerging avenue in biomedical and biomedical engineering opportunities. J Adv Res 2021.

[36] Frederix F, Friedt J-M, Choi K-H, Laureyn W, Campitelli A, Mondelaers D, et al. Biosensing based on light absorption of nanoscaled gold and silver particles. Anal Chem 2003;75(24):6894–900.

[37] Kunzmann A, Andersson B, Thurnherr T, Krug H, Scheynius A, Fadeel B. Toxicology of engineered nanomaterials: focus on biocompatibility, biodistribution and biodegradation. Biochim Biophys Acta (BBA) – General Subjects 2011;1810(3):361–73.

[38] Gangishetty MK, Scott RW, Kelly TL. Thermal degradation mechanism of triangular Ag@ SiO2 nanoparticles. Dalton Trans 2016;45(24):9827–34.

[39] George A, Sanjay MR, Srisuk R, Parameswaranpillai J, Siengchin S. A comprehensive review on chemical properties and applications of biopolymers and their composites. Int J Biol Macromol 2020;154:329–38.

[40] Jahan Z, Niazi MBK, Gregersen ØW. Mechanical, thermal and swelling properties of cellulose nanocrystals/PVA nanocomposites membranes. J Ind Eng Chem 2018;57:113–24.

[41] Teodorescu M, Bercea M, Morariu S. Biomaterials of poly (vinyl alcohol) and natural polymers. Polym Rev 2018;58(2):247–87.

[42] Kyrychenko A, Pasko DA, Kalugin ON. Poly (vinyl alcohol) as a water protecting agent for silver nanoparticles: The role of polymer size and structure. PCCP 2017;19(13):8742–56.

[43] Homan KA, Souza M, Truby R, Luke GP, Green C, Vreeland E, et al. Silver nanoplate contrast agents for in vivo molecular photoacoustic imaging. ACS Nano 2012;6(1):641–50.

[44] Liu X, Lin J, Jiang TF, Zhu ZF, Zhan Q, Qian J, et al. Surface plasmon properties of hollow AuAg alloyed triangular nanoboxes and its applications in SERS imaging and potential drug delivery. Prog Electromagnet Res 2012;128:35–53.

[45] Zeng X, Yan S, Di C, Lei M, Chen P, Du W, et al. "All-in-One" Silver nanoprism platform for targeted tumor theranostics. ACS Appl Mater Interfaces 2020;12(10):11329–40.

[46] Zhang Q, Li N, Goebl J, Lu Z, Yin Y. A systematic study of the synthesis of silver nanoplates: is citrate a "magic" reagent? J Am Chem Soc 2011;133(46):18931–9.

[47] Manivasagan P, Jun SW, Hoang G, Mondal S, Kim H, Doan VHM, et al. Anti-EGFR antibody conjugated thiol chitosan-layered gold nanoshells for dual-modal imaging-guided cancer combination therapy. J Control Release 2019;311:26–42.

[48] Bharathiraja S, Bui NQ, Manivasagan P, Moorthy MS, Mondal S, Seo H, et al. Multimodal tumor-homing chitosan oligosaccharide-coated biocompatible palladium nanoparticles for photo-based imaging and therapy. Sci Rep 2018;8(1):1–16.

[49] Henglein A. Physicochemical properties of small metal particles in solution:" microelectrode" reactions, chemisorption, composite metal particles, and the atom-to-metal transition. J Phys Chem 1993;97(21):5457–71.

[50] Shahjamali MM, Zhou Y, Zaraee N, Xue C, Wu J, Large N, et al. Ag–Ag2S hybrid nanoprisms: structural versus plasmonic evolution. ACS Nano 2016;10(5):5362–73.

[51] Jyoti K, Baunthiyal M, Singh A. Characterization of silver nanoparticles synthesized using Urtica dioica Linn. leaves and their synergistic effects with antibiotics. J Radiat Res Appl Sci 2016;9(3):217–27.

[52] Liu X, Li B, Fu F, Xu K, Zou R, Wang Q, et al. Facile synthesis of biocompatible cysteine-coated CuS nanoparticles with high photothermal conversion efficiency for cancer therapy. Dalton Trans 2014;43(30):11709–15.

[53] Espinosa A, Curcio A, Cabana S, Radtke G, Bugnet M, Kolosnjaj-Tabi J, et al. Intracellular biodegradation of Ag nanoparticles, storage in ferritin, and protection by a Au shell for enhanced photothermal therapy. ACS Nano 2018;12(7):6523–35.

[54] Chen J, Glaus C, Laforest R, Zhang Q, Yang M, Gidding M, et al. Gold nanocages as photothermal transducers for cancer treatment. Small 2010;6(7):811–7.

[55] <https://www.lumerical.com/products/.>

[56] Palik ED. Handbook of optical constants of solids. Academic press; 1998.

[57] Manrique-Bedoya S, Abdul-Moqueet M, Lopez P, Gray T, Disiena M, Locker A, et al. Multiphysics modeling of plasmonic photothermal heating effects in gold nanoparticles and nanoparticle arrays. J Phys Chem C 2020;124(31):17172–82.

[58] Baffou G, Quidant R. Thermo-plasmonics: using metallic nanostructures as nano-sources of heat. Laser Photonics Rev 2013;7(2):171–87.

[59] Terentyuk GS, Akchurin GG, Maksimova IL, Maslyakova GN, Khlebtsov NG, Tuchin VV. Cancer laser thermotherapy mediated by plasmonic nanoparticles. In: Handbook of photonics for biomedical science. CRC Press; 2010. p. 799–834.

[60] Biris AS, Boldor D, Palmer J, Monroe WT, Mahmood M, Dervishi E, et al. Nanophotothermolysis of multiple scattered cancer cells with carbon nanotubes guided by time-resolved infrared thermal imaging. J Biomed Opt 2009;14(2):021007.

[61] Ma Z, Han K, Dai X, Han H. Precisely striking tumors without adjacent normal tissue damage via mitochondria-templated accumulation. ACS Nano 2018;12(6):6252–62.

[62] Chen C, Wang S, Li L, Wang P, Chen C, Sun Z, et al. Bacterial magnetic nanoparticles for photothermal therapy of cancer under the guidance of MRI. Biomaterials 2016;104:352–60.

[63] Soo Choi H, Liu W, Misra P, Tanaka E, Zimmer JP, Itty Ipe B, et al. Renal clearance of quantum dots. Nat Biotechnol 2007;25(10):1165–70.

[64] Poon W, Zhang Y-N, Ouyang B, Kingston BR, Wu JL, Wilhelm S, et al. Elimination pathways of nanoparticles. ACS Nano 2019;13(5):5785–98.